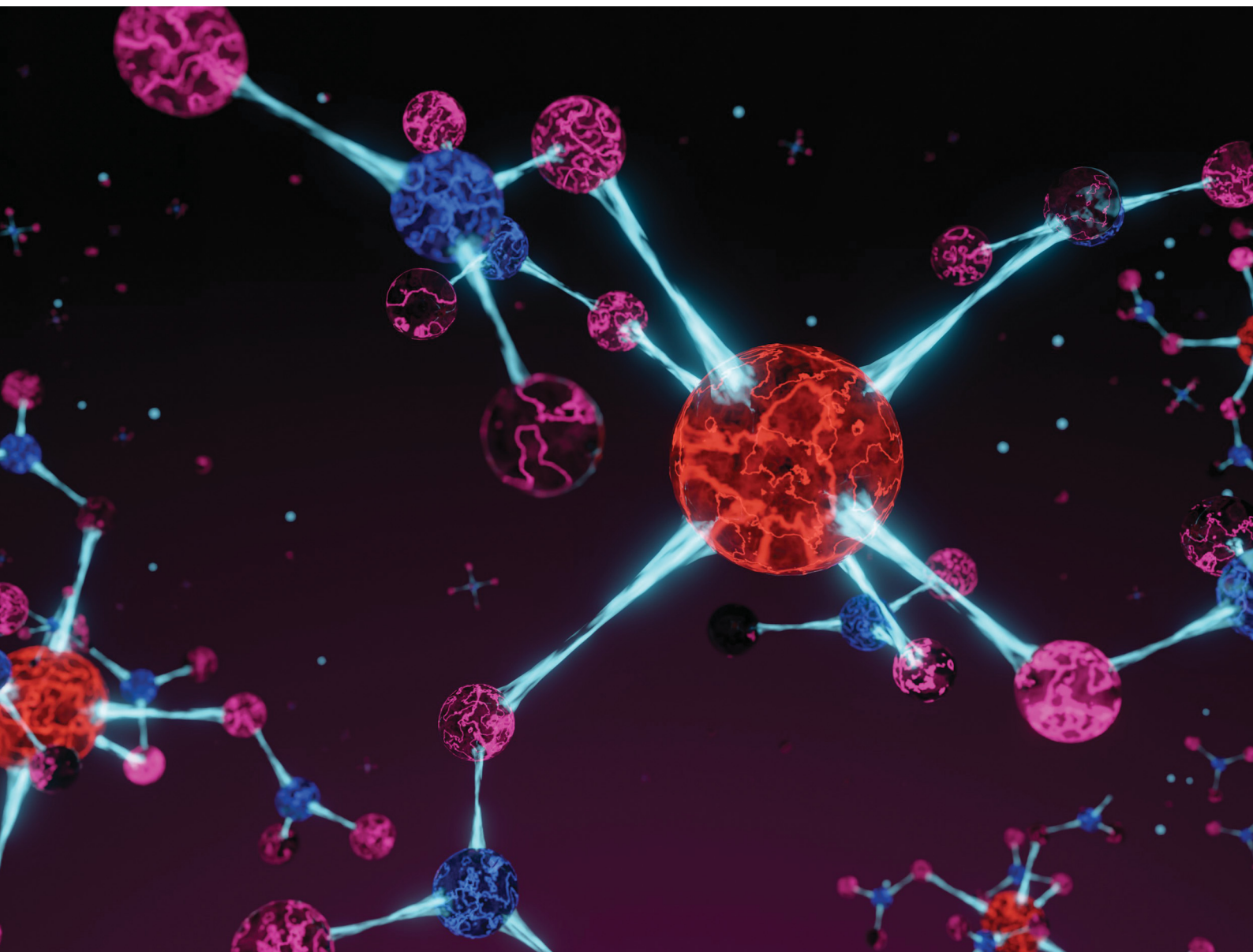


# Materials Advances

Volume 4  
Number 8  
21 April 2023  
Pages 1787–2018

[rsc.li/materials-advances](https://rsc.li/materials-advances)



ISSN 2633-5409

**PAPER**

M. Veronica Sofianos *et al.*  
Upcycling natural Limestone waste for thermochemical  
energy storage by utilising tailored  $\text{CaZrO}_3$  nanoadditives

Cite this: *Mater. Adv.*, 2023,  
4, 1905

## Upcycling natural Limestone waste for thermochemical energy storage by utilising tailored $\text{CaZrO}_3$ nanoadditives†

Rehan Anwar,<sup>a</sup> Jan Navrátil,<sup>ib bc</sup> Rajani K. Vijayaraghavan,<sup>ib d</sup>  
Patrick J. McNally,<sup>ib d</sup> Michal Otyepka,<sup>ib be</sup> Piotr Błoński<sup>ib b</sup> and  
M. Veronica Sofianos<sup>ib \*a</sup>

The development of long-term renewable energy storage systems is crucial for decarbonising the energy sector and enabling the transition to a sustainable energy future. Thermochemical energy storage (TCES) systems are well suited for long-term renewable energy storage as the materials used in these systems have high energy densities, and long storage duration. Among the plethora of TCES materials, calcium carbonate (Limestone) is of particular interest since it exhibits a high enthalpy of reaction, and it is earth-abundant. The main problem with Limestone inhibiting its commercial application for long-term renewable energy storage is its deteriorating cycling performance after several energy charge/discharge cycles. In this study, two  $\text{CaZrO}_3$  nanoadditives with two different Ca:Zr ratios and tailored oxygen vacancies were synthesised by a precipitation method, and mixed with Limestone waste at three weight concentrations (5, 10 and 20 wt%). Their phase, chemical state and morphology were determined by XRD, XPS and TEM, respectively. The cycling performance of the mixture samples was determined through thermogravimetric analysis. The best performing sample was the one mixed with 20%  $\text{CaZrO}_3$  nanoadditives, which contained a large number of oxygen vacancies and thus had enhanced ionic conductivity, as confirmed by density functional theory (DFT) calculations. This sample exhibited the best effective conversion and the highest energy density values of 0.7 and 2640  $\text{kJ kg}^{-1}$ , respectively, after 40 cycles.

Received 14th December 2022,  
Accepted 24th February 2023

DOI: 10.1039/d2ma01083f

rsc.li/materials-advances

### Introduction

Long-term energy storage is essential if renewable energy is to replace the use of fossil fuels and meet global energy demands.<sup>1</sup> Due to its intermittent nature, reliable and continuous renewable power-to-grid supply cannot be ensured, therefore long-term energy storage is crucial. There are a number of long-term energy storage systems that can address the renewable energy

intermittency, the most popular being flow batteries,<sup>2</sup> pumped hydro energy storage,<sup>3</sup> and thermal energy storage. Thermal energy storage (TES) is considered one of the most promising energy storage systems due to its affordability and efficiency.<sup>4,5</sup>

There are three types of TES systems based on their energy storage mode: sensible heat storage (SHS), latent heat storage (LHS) and thermochemical energy storage (TCES).<sup>6,7</sup> SHS uses temperature changes of a material to store heat energy. SHS systems have low energy densities (72–108  $\text{kJ kg}^{-1}$ ) and limited storage duration due to thermal losses.<sup>8</sup> In LHS systems, phase change materials are used to store heat energy. When these materials change their phase, they absorb/release heat. LHS systems possess relatively larger energy densities (108–360  $\text{kJ kg}^{-1}$ ) to SHS, but have a limited storage duration associated with thermal losses.<sup>9</sup> TCES systems utilize reversible chemical reactions for heat energy storage.<sup>10</sup> TCES is the most promising TES system as the materials used have higher energy densities (1800–3600  $\text{kJ kg}^{-1}$ ) in comparison to the other two systems and long-term storage duration.<sup>11</sup>

As mentioned before, TCES systems utilize reversible chemical reactions for storing heat. During their endothermic

<sup>a</sup> School of Chemical and Bioprocess Engineering, University College Dublin, Belfield, Dublin 4, Ireland. E-mail: mvsofianou@gmail.com

<sup>b</sup> Regional Centre of Advanced Technologies and Materials, Czech Advanced Technology and Research Institute (CATRIN), Palacký University, Šlechtitelů 27, 783 71, Olomouc, Czech Republic

<sup>c</sup> Department of Physical Chemistry, Faculty of Science, Palacký University, 17. listopadu 1192/12, 779 00 Olomouc, Czech Republic

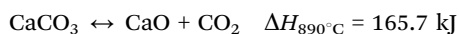
<sup>d</sup> School of Electronic Engineering, Dublin City University, Glasnevin, Dublin 9, Ireland

<sup>e</sup> IT4Innovations, Technical University of Ostrava, 708 00 Ostrava-Poruba, Czech Republic

† Electronic supplementary information (ESI) available:  $\text{CO}_2$  uptake/release capacity data, EDS mapping, SEM micrograph, computational details, DFT results. See DOI: <https://doi.org/10.1039/d2ma01083f>



reactions, heat is stored while heat is released during their reverse exothermic reactions.<sup>12</sup> Metal carbonates,<sup>13–16</sup> hydrides,<sup>17–20</sup> and hydroxides<sup>12,21</sup> are commonly used materials for TCES systems.<sup>22</sup> Calcium carbonate (CaCO<sub>3</sub>), also known as Limestone, has a high enthalpy of (calcination/carbonation) reaction ( $\Delta H_{890^\circ\text{C}} = 165.7 \text{ kJ}$ ), it is easy to handle and transport, has a high energy storage density ( $>1000 \text{ kJ kg}^{-1}$ ) and is earth-abundant, making it a very attractive candidate for storing renewable energy long-term.<sup>4,23,24</sup> CaCO<sub>3</sub> dissociates into CaO and CO<sub>2</sub> by absorbing heat (calcination), and can theoretically release the same amount of heat during the reverse reaction (carbonation).<sup>25,26</sup>



Unfortunately, Limestone has very slow reaction kinetics during charge/discharge (cycling), and its energy storage capacity degrades upon consecutive energy charge/discharge cycles. It is believed that these drawbacks are related to sintering phenomena, and poor ionic mobility of Ca<sup>2+</sup>, O<sup>2-</sup> and CO<sub>3</sub><sup>2-</sup> at high temperatures.<sup>30–32</sup>

According to the literature, a plethora of additives have been used as an effective way to enhance the cycling performance of Limestone, including Al<sub>2</sub>O<sub>3</sub>,<sup>33–35</sup> SiO<sub>2</sub>,<sup>36–38</sup> and ZrO<sub>2</sub>.<sup>27–29,39–41</sup> Among these additives, ZrO<sub>2</sub> has been the most promising. In most published studies it was reported, that ZrO<sub>2</sub> converts to CaZrO<sub>3</sub> during cycling (Table 1), stating that this ternary oxide plays the key role in improving the cycling performance of Limestone.

CaZrO<sub>3</sub> is a perovskite with a high melting point (2345 °C), small thermal expansion coefficient, high strength, excellent corrosion resistance against alkali oxides, and is chemically and thermally stable at high temperatures.<sup>42</sup> Due to its perovskite structure, it possess a high ionic conductivity, promoting ionic diffusion during catalytic reactions.<sup>43</sup> CaZrO<sub>3</sub> has been reported to have been used for catalytic ozonation, CO<sub>2</sub> capturing, sensing humidity, and in dielectric applications.<sup>43–46</sup>

To the best of our knowledge, this is the first study to use tailored CaZrO<sub>3</sub> nanoadditives for upcycling natural Limestone waste for thermochemical energy storage. The CaZrO<sub>3</sub> nanoparticles were synthesized using a wet precipitation method and were systematically characterized using both experimental and computational methods. Their morphology, specific surface area and chemical composition were determined by SEM/TEM, BET analysis, and XRD/XPS respectively. Their ionic conductivity was studied theoretically in the framework of DFT, determining

Table 1 Performance of ZrO<sub>2</sub> as an additive to CaCO<sub>3</sub> based TCHS

Additive	Wt % additive	Formed product	Ref.
ZrO <sub>2</sub>	20	CaZrO <sub>3</sub>	27
ZrO <sub>2</sub>	5	CaZrO <sub>3</sub>	28
ZrO <sub>2</sub>	15	CaZrO <sub>3</sub>	28
ZrO <sub>2</sub>	30	CaZrO <sub>3</sub>	28
ZrO <sub>2</sub>	20	CaZrO <sub>3</sub>	29
ZrO <sub>2</sub>	40	CaZrO <sub>3</sub>	29
ZrO <sub>2</sub>	5	CaZrO <sub>3</sub>	40
ZrO <sub>2</sub>	5	Not reported	41

energy barriers for their transport in the studied systems. These tailored nanoparticles were mixed with Limestone waste in three different weight percentages (5, 10 and 20 wt%). How the difference in ionic conductivity, particle size, specific surface area and weight concentration of the CaZrO<sub>3</sub> nanoadditives influence the cycling stability and thermochemical energy storage properties of Limestones was reported.

## Experimental

### Synthesis of CaZrO<sub>3</sub> nanoadditives

CaZrO<sub>3</sub> nanoparticles were synthesized using a wet precipitation method. Specifically, two samples, CaZrO<sub>3</sub>-I and CaZrO<sub>3</sub>-II, were prepared using two different stoichiometric ratios of Ca to Zr as seen in (Table 2). Stoichiometrically calculated amounts of CaCl<sub>2</sub>·2H<sub>2</sub>O (>99%, Honeywell) and ZrOCl<sub>2</sub>·8H<sub>2</sub>O (98%, ACROS ORGANICS) were dissolved in ethanol, and then mixed together under continuous magnetic stirring to obtain a uniform solution. Specific amounts of NaOH (>97%, SIGMA-ALDRICH) were added to the above solution to obtain an overall molarity of 0.5 M for the final solution. The solution was then kept at 50 °C for 24 h under constant stirring. The resulting white precipitates were collected by centrifugation, dried in an oven at 110 °C for 24 h, and then further calcined at 1000 °C for 3.5 h with a 3 °C min<sup>-1</sup> heating rate Fig. 1.

### CaZrO<sub>3</sub>/Limestone sample preparation

The CaZrO<sub>3</sub>/Limestone samples were prepared by physically mixing CaZrO<sub>3</sub> nanoparticles and Limestone waste (Bennetts-bridge Limestone Quarries, Ireland) in three different weight percentages (Table 3) using a mortar and pestle. Limestone waste was heated at 500 °C for two hours prior to further use in order to remove any impurities. More details can be found in the thermal analysis of natural Limestone section.

### Materials characterization

**X-ray diffraction.** Phase observations of the samples before and after calcination/carbonation cycling were conducted by *ex situ* powder X-ray diffraction (XRD) using a Siemens D500 (40 kV, 30 mA) diffractometer from Germany with a Cu Ka

Table 2 Sample ID and stoichiometric ratio for CaZrO<sub>3</sub> samples

Sample ID	Stoichiometric ratio (Ca : Zr)
CaZrO <sub>3</sub> -I	1 : 1
CaZrO <sub>3</sub> -II	0.9 : 1

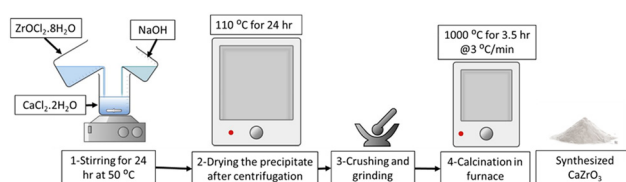


Fig. 1 Illustration of the CaZrO<sub>3</sub> nanoparticle synthesis method.



**Table 3** Additive percentage and sample ID of CaZrO<sub>3</sub>/Limestone samples

Sample description	Sample IDs	
	Before cycling	After cycling
100% Limestone waste	Lim BBL	40_Lim BBL
5% CaZrO <sub>3</sub> -I + 95% Limestone waste	5R1	40_5R1
10% CaZrO <sub>3</sub> -I + 90% Limestone waste	10R1	40_10R1
20% CaZrO <sub>3</sub> -I + 80% Limestone waste	20R1	40_20R1
5% CaZrO <sub>3</sub> -II + 95% Limestone waste	5R0.9	40_5R0.9
10% CaZrO <sub>3</sub> -II + 90% Limestone waste	10R0.9	40_10R0.9
20% CaZrO <sub>3</sub> -II + 80% Limestone waste	20R0.9	40_20R0.9

radiation ( $\lambda = 1.5405 \text{ \AA}$ ). All measurements were taken in a  $10\text{--}80^\circ$   $2\theta$  range with a  $0.03^\circ$  step size, a 2 s per step scan speed and a 30 rpm rotational speed. *In situ* powder X-ray diffraction was performed on the 20R1 and 20R0.9 samples using a triple-axis Jordan Valley Bede D1 high-resolution XRD system with a copper ( $\lambda = 1.5405 \text{ \AA}$ ) radiation source operated at 45 kV and 40 mA. Bede D1 system was equipped with an Anton Paar DHS 1100 heating stage, which allowed *in situ* temperature dependent measurements in a vacuum environment. The powder samples were pressed in a pellet with a 20 mm diameter and 2 mm in thickness, and then mounted onto the heating stage. XRD measurements were carried out at various temperatures starting from room temperature (RT) to  $1000^\circ\text{C}$ . The heating rate was  $500^\circ\text{C min}^{-1}$  for heating from RT– $500^\circ\text{C}$  and  $800\text{--}1000^\circ\text{C}$ . Whereas for heating from  $500\text{--}800^\circ\text{C}$ , the heating rate was  $20^\circ\text{C min}^{-1}$ . The measurements were performed using the  $\theta\text{--}2\theta$  configuration between  $20^\circ$  and  $40^\circ$ , with a step size of  $0.1^\circ$  and each scan took approximately 13 min.

### Scanning electron microscopy

A Zeiss Sigma 300 scanning electron microscope (SEM) was used for morphological observations. SEM specimens were prepared by placing a small amount of powder onto carbon tape and then coating them with a 4 nm layer of platinum to produce a conductive layer and reduce charging during SEM imaging. EDS mapping was done on a Hitachi Regulus 8230 Field Emission Gun Scanning Electron Microscope (FEGSEM) coupled with an Oxford Astec 170 EDS and manipulated by the Aztec software.

### Transmission electron microscopy

A high-resolution transmission electron microscope (HR-TEM) was used to observe the CaZrO<sub>3</sub> nanoparticles using a Tecnai 20

TEM with an acceleration voltage of 200 kV. TEM samples were prepared on copper grids by placing few drops of suspension (CaZrO<sub>3</sub> nanoparticles and ethanol) and dried under an IR lamp for 20–30 seconds.

### Brunauer–Emmett–Teller method

Specific surface area calculations for all samples were performed by applying nitrogen (N<sub>2</sub>) adsorption at 77 K using a Micromeritics Gemini VII system (Micromeritics, Nor-cross, GA, USA), and employing the Brunauer–Emmett–Teller (BET) multi-point method using the relative pressures between 0.05 and 0.30 bar. All samples were outgassed at  $200^\circ\text{C}$  under a nitrogen atmosphere prior to their N<sub>2</sub> adsorption analysis.

### X-ray photoelectron spectroscopy

The CaZrO<sub>3</sub> samples were also tested by X-ray photoelectron spectroscopy (XPS), using a Kratos AXIS Ultra DLD X-ray photoelectron spectrometer in ultra-high vacuum equipped with an Al K<sub>2</sub> X-ray source (1486.7 eV). The data was analyzed using the Casa XPS software and calibrated using the surface adventitious C 1s peak at 284.5 eV.

### Density functional theory calculations

All calculations in this work were performed in the DFT framework, as implemented in the plane-wave Vienna *ab initio* simulation package (VASP).<sup>47–50</sup> The basis set was limited to plane waves with a maximum kinetic energy of 400 eV. The electron–ion interactions were treated by the projected augmented wave (PAW) method.<sup>51,52</sup> The electronic exchange and correlation effects were handled at the generalized-gradient approximation (GGA) level using the functional of Perdew, Burke and Ernzerhof (PBE).<sup>53,54</sup> Grimme's zero-damping DFT-D3 method was used to account for London dispersion interactions.<sup>55</sup> The electronic degrees of freedom were relaxed by a preconditioned conjugate gradient algorithm with an electronic energy convergence threshold set at  $10^{-6}$  eV. For Brillouin zone sampling, after convergence tests (Table S1, ESI<sup>†</sup>), a  $\Gamma$ -centred  $2 \times 2 \times 2$   $k$ -point mesh was used.

Initially, two structures of CaZrO<sub>3</sub> shown in Fig. 2, orthorhombic and cubic, were considered. Since the former is  $\sim 0.2$  eV per atom more stable than the latter, it was used in further calculations.

The structures were optimized, including the lattice constants, by the conjugate gradient algorithm until all forces acting on the atoms were reduced to less than  $0.02 \text{ eV \AA}^{-1}$ .

Structures were visualized using VESTA<sup>56</sup> or Speck.<sup>57</sup> All other calculation details can be found in Section S2 (ESI<sup>†</sup>).

### Thermogravimetric analysis

Thermogravimetric analysis of Limestone was performed on a TA Q500 instrument. For this measurement, 30–35 mg of powder Limestone was placed in a Pt crucible. Firstly, the sample was heated from room temperature to  $1000^\circ\text{C}$  under a N<sub>2</sub> flow ( $100 \text{ mL min}^{-1}$ ) with a  $20^\circ\text{C min}^{-1}$  and was kept isothermal for 20 min under a CO<sub>2</sub>/N<sub>2</sub> flow (CO<sub>2</sub> at  $90 \text{ mL min}^{-1}$

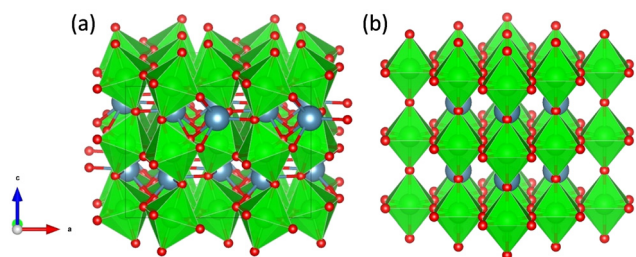


**Fig. 2** Orthorhombic (a) and cubic (b) structure of CaZrO<sub>3</sub>. Ca, Zr and O atoms are represented by blue, green and red spheres, respectively. ZrO<sub>6</sub> octahedra are indicated in green.



and N<sub>2</sub> at 10 mL min<sup>-1</sup>) and cooled down to room temperature with a 20 °C min<sup>-1</sup> cooling rate under the same atmosphere.

### Calcination/carbonation cycling and heat storage performance

Calcination and carbonation cycles were performed using a thermogravimetric analyzer Q500 by TA instruments at a constant temperature of 884 °C. The calcination step was performed under a 100 mL min<sup>-1</sup> N<sub>2</sub> flow with 10 min dwell time, whereas the carbonation step took place under a mixture of 90 mL min<sup>-1</sup> CO<sub>2</sub> and 10 mL min<sup>-1</sup> N<sub>2</sub> flow with 20 min dwell time. At the start of the cycling measurements, all samples were heated from room temperature to 884 °C under a N<sub>2</sub> flow (100 mL min<sup>-1</sup>) with a 20 °C min<sup>-1</sup> heating rate. At the end of the cycling, all samples were cooled down to room temperature under a CO<sub>2</sub>/N<sub>2</sub> flow (CO<sub>2</sub> at 90 mL min<sup>-1</sup> and N<sub>2</sub> at 10 mL min<sup>-1</sup>) with a 20 °C min<sup>-1</sup> cooling rate.

The heat storage performance of all samples was evaluated by the effective conversion, and the heat storage density. The effective conversion,  $X_{\text{ef},N}$ , represents the ratio of the mass of CaO that has reacted during each carbonation step (cycle) to the total mass of the sample before the carbonation, as defined by eqn (1):

$$X_{\text{ef},N} = \frac{m_{\text{car},N} - m_{\text{cal},N-1}}{m_0} \cdot \frac{M_{\text{CaO}}}{M_{\text{CO}_2}} \quad (1)$$

where  $N$  is the number of calcination/carbonation cycles,  $m_{\text{car},N}$  and  $m_{\text{cal},N-1}$  is the mass of the sample after the  $N$ th carbonation and the  $N - 1$ th calcination in g, respectively.  $m_0$  is the original mass of the sample including the mass of any additives used in g,  $M_{\text{CaO}}$  and  $M_{\text{CO}_2}$  represent the molar masses of CaO and CO<sub>2</sub> in g mol<sup>-1</sup>, correspondingly.

Heat storage density,  $E_{\text{g},N}$ , in kJ kg<sup>-1</sup>, denotes the maximum heat that can be released per unit mass of the samples during each carbonation reaction, as defined by eqn (2):

$$E_{\text{g},N} = X_{\text{ef},N} \cdot \frac{1000\Delta H^\circ}{M_{\text{CaO}}} \quad (2)$$

where  $\Delta H^\circ$  is the standard enthalpy of reaction for 890 °C is equal to 165.7 kJ mol<sup>-1</sup>.

## Results and discussion

### Phase and morphological observations and specific surface area calculations of CaZrO<sub>3</sub>

XRD patterns of the CaZrO<sub>3</sub>-I and CaZrO<sub>3</sub>-II samples are presented in Fig. 3. The predominant phase corresponds to CaZrO<sub>3</sub> (PDF 96-153-2748). It is suspected that due to the higher stoichiometric ratio of Zr to Ca in the CaZrO<sub>3</sub>-II sample, a secondary phase of ZrO<sub>2</sub> (PDF 96-900-9052) with peaks identified at 30° and 35°  $2\theta$  is present.<sup>58</sup> A CaO peak for the CaZrO<sub>3</sub>-I sample at 30°  $2\theta$  is present in its diffraction pattern due to unreacted CaO (PDF 96-900-6747).<sup>59</sup>

The as-synthesised CaZrO<sub>3</sub> nanoparticles can be observed in the SEM (Fig. 4(a) and (c)) and TEM (Fig. 4(b) and (d)) micrographs. It is noticeable that the size of the nanoparticles is polydisperse in both CaZrO<sub>3</sub> samples. As the final synthesis step was calcination of the dried precipitates at 1000 °C,

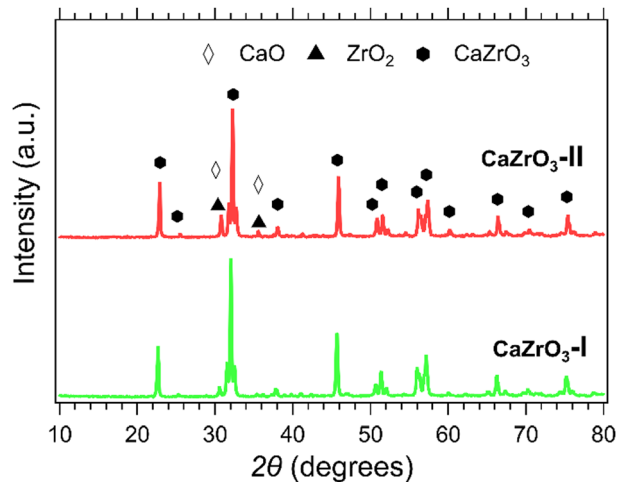


Fig. 3 XRD patterns of CaZrO<sub>3</sub>-I (green) and CaZrO<sub>3</sub>-II (red). Peaks of CaO are represented with the white diamond marker and ZrO<sub>2</sub> with the black triangle marker.

sintering of some nanoparticles can be observed in both samples. Despite this, all the CaZrO<sub>3</sub> particles are still in the nanometre range.

The BET surface area was  $8.99 \pm 0.9$  and  $6.43 \pm 0.6$  m<sup>2</sup> g<sup>-1</sup> for the CaZrO<sub>3</sub>-I and CaZrO<sub>3</sub>-II respectively. According to Andre *et al.*,<sup>59</sup> excess of Zr during synthesis leads to higher grain sizes, which explains the lower BET values for the CaZrO<sub>3</sub>-II sample. The average particle size for CaZrO<sub>3</sub>-I was 72.88 nm and for CaZrO<sub>3</sub>-II was 68.22 nm as calculated from their associated TEM images.

### XPS analysis of CaZrO<sub>3</sub>

It can be observed in Fig. 5(a) and (d) that two peaks are present in the high-resolution Ca 2p spectra. One at ~346.25 eV and the other at ~349.75 eV, corresponding to Ca 2p<sub>3/2</sub> and Ca 2p<sub>1/2</sub>.<sup>56</sup> Two peaks are also present in the high resolution Zr 3d

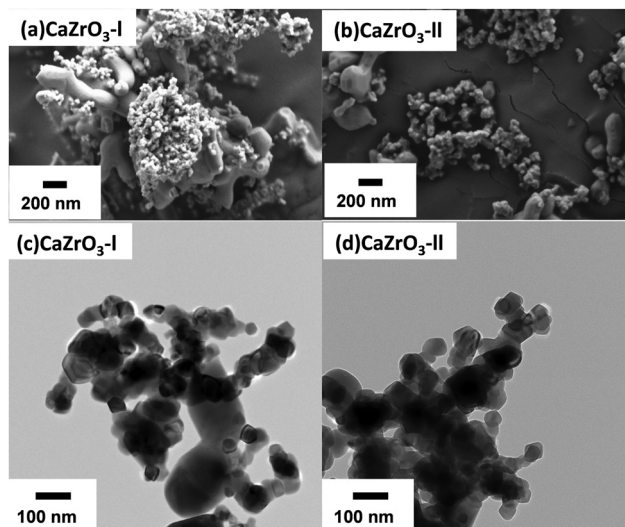


Fig. 4 SEM (a), (b) and TEM (c), (d) images of CaZrO<sub>3</sub>-I and CaZrO<sub>3</sub>-II.



spectra; the first at  $\sim 181.50$  eV assigned to Zr  $3d_{5/2}$  and the second at  $\sim 183.87$  eV assigned to Zr  $3d_{3/2}$  (Fig. 5(b) and (e)).<sup>59,60</sup> In the O 1s high resolution spectra, two peaks at  $\sim 529.5$  eV and  $\sim 531.5$  eV are noticeable, corresponding to the oxygen lattice ( $O_{\text{lat}}$ ) and the oxygen vacancies ( $O_{\text{vac}}$ ) (Fig. 5(c) and (f)).<sup>61,62</sup> Table 4 displays the actual binding energy values of Ca 2p, Zr 3d and O 1s for the CaZrO<sub>3</sub>-I and CaZrO<sub>3</sub>-II samples, along with standard binding energy values. Due to the increase of Zr content in the CaZrO<sub>3</sub>-II sample, the binding energy values of Ca 2p and Zr 3d are shifted towards lower binding energies.<sup>56</sup> On the contrary, the O1s binding energy values shifted towards higher values due to access Zr.<sup>56</sup> Moreover, the percentage of  $O_{\text{vac}}$  of the CaZrO<sub>3</sub>-I and CaZrO<sub>3</sub>-II samples were calculated to be 23.43% and 28.58%. The high percentage of  $O_{\text{vac}}$  is expected to improve the ionic conductivity of CaZrO<sub>3</sub>, which is confirmed by DFT calculations presented later in the article.

### DFT calculations of defect formation in CaZrO<sub>3</sub>

The formation of CaZrO<sub>3</sub> in the reaction  $\text{CaO} + \text{ZrO}_2 \rightarrow \text{CaZrO}_3$  instead of separated CaO and ZrO<sub>2</sub> is associated with an energy gain of 0.06 eV per atom calculated on the basis of the total energies of reactants and products. Such a small difference in energy explains why all three components are formed during synthesis.

Next, the formation of a single atomic vacancy in a bulk CaZrO<sub>3</sub> crystal was considered. This is energetically unfavourable by 6.8 eV, 3.4 eV, and 5.9 eV, respectively, for the missing O, Ca, and Zr atom in the Ca<sub>4</sub>Zr<sub>4</sub>O<sub>12</sub> supercell and by 8.0 eV, 3.9 eV, and 6.5 eV in the Ca<sub>32</sub>Zr<sub>32</sub>O<sub>96</sub> supercell. This indicates that the formation of atomic vacancy defects is more favourable with higher densities of such defects, which was further confirmed

by the calculations of two missing O atoms at different positions in the Ca<sub>32</sub>Zr<sub>32</sub>O<sub>96</sub> supercell, showing that defect formation energy decreases to 7.0–7.5 eV per the missing O atom. It can also be seen that Ca defects can be formed more easily than Zr defects due to the number of their valence electrons; the missing Ca atom with two valence electrons causes less change in its vicinity compared to the Zr atom with four valence electrons.

Both the excess of Ca and Zr atoms in interstitial positions and the replacement of O atoms were also taken into account. Both scenarios, however, are energetically very unfavourable (Table S2, ESI<sup>†</sup>).

In addition, multiple defects in the crystal represented by the Ca<sub>12</sub>Zr<sub>12</sub>O<sub>36</sub> supercell were created focusing on four stoichiometries, Ca<sub>12</sub>Zr<sub>11</sub>O<sub>28</sub>, Ca<sub>12</sub>Zr<sub>10</sub>O<sub>28</sub>, Ca<sub>12</sub>Zr<sub>12</sub>O<sub>28</sub>, and Ca<sub>11</sub>Zr<sub>12</sub>O<sub>26</sub> with the latter two corresponding to experimental samples CaZrO<sub>3</sub>-I and CaZrO<sub>3</sub>-II. The two most important structures are shown in Fig. 6, all considered structures are shown in Section S3 (ESI<sup>†</sup>). Their relative energies to the structural ground state (GS) in systems of the same stoichiometry are in the range 0.5–2.9 eV. They are less than the defect formation energy of a single O vacancy and given the bottom-up approach used in the synthesis, many of these defects are likely to develop considering that this is a stochastic process. Moreover, bulk defects are preferred to a series of single defects in the crystal, which has a significant impact on the ionic conductivity of this material (*vide infra*), and the least stable defects contain significantly undercoordinated metal atoms.

Finally, the formation of multiple vacancies at the (001) surface of CaZrO<sub>3</sub> (Fig. 6 and Section S3, ESI<sup>†</sup>) was investigated. Two stoichiometries of Ca<sub>32</sub>Zr<sub>32</sub>O<sub>75</sub> and Ca<sub>29</sub>Zr<sub>32</sub>O<sub>69</sub> were considered, corresponding to the experimental systems CaZrO<sub>3</sub>-I and CaZrO<sub>3</sub>-II, respectively. Although the (110) surface may also be present in experimental samples (Table S4, ESI<sup>†</sup>), the focus was on the former surface because the atomic vacancies present there have a similar formation energy as in the bulk crystal (Table S5, ESI<sup>†</sup>), and thus the latter surface may be similar. The most energetically favourable defects create a crater-like structure at the (001) surface, while a long narrow channel through the whole slab is less favourable (Table S5, ESI<sup>†</sup>). Their role in ion conductivity is discussed below.

### Thermal analysis of natural Limestone waste

Thermal analysis of the natural Limestone waste (Fig. 7) was performed to identify the exact temperatures at which the calcination and carbonation reactions take place. This information is crucial for determining the correct parameters that need to be applied for the cycling experiments. A 20% weight loss was observed between 350 °C to 590 °C which may be due to the decomposition of impurities present in the Limestone waste, since it was measured as received from the quarry with no further treatment (Fig. 7(a)). The second weight loss, from 80% down to 45%, between 610 °C and 910 °C is linked to the decomposition of Limestone to CO<sub>2</sub> and CaO (Fig. 7(a)). This decomposition reaction is also known as calcination reaction, with a peak maximum observed at 785 °C (Fig. 7(b)). The Limestone sample was then kept isothermal at 1000 °C under a 90% CO<sub>2</sub> atmosphere for

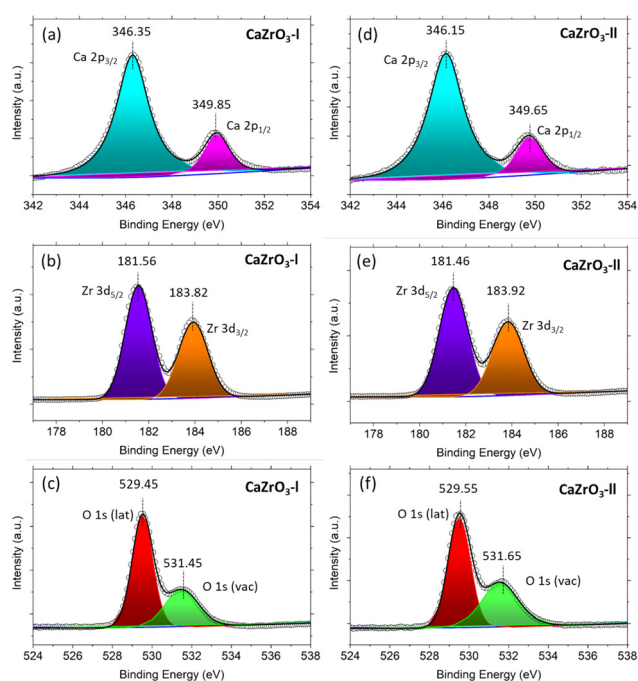


Fig. 5 XPS spectra of CaZrO<sub>3</sub>-I and CaZrO<sub>3</sub>-II: (a) Ca 2p-I, (b) Zr 3d-I, (c) O 1s-I, (d) Ca 2p-II, (e) Zr 3d-II, (f) O 1s-II.



Table 4 Binding energy values (eV) for CaZrO<sub>3</sub>-I and CaZrO<sub>3</sub>-II determined by XPS

Sample name	Ca 2p	Ca 2p	Zr 3d <sub>2</sub>	Zr 3d <sub>3/2</sub>	O 1s (lattice)	O1s (vacancy)
CaZrO <sub>3</sub> -I	346.35	349.85	181.56	183.92	529.45	531.45
CaZrO <sub>3</sub> -II	346.15	349.65	181.46	183.82	529.55	531.65
Standard values <sup>60,64</sup>	346–347	348–350	181–182	183–185	529–530	531–532

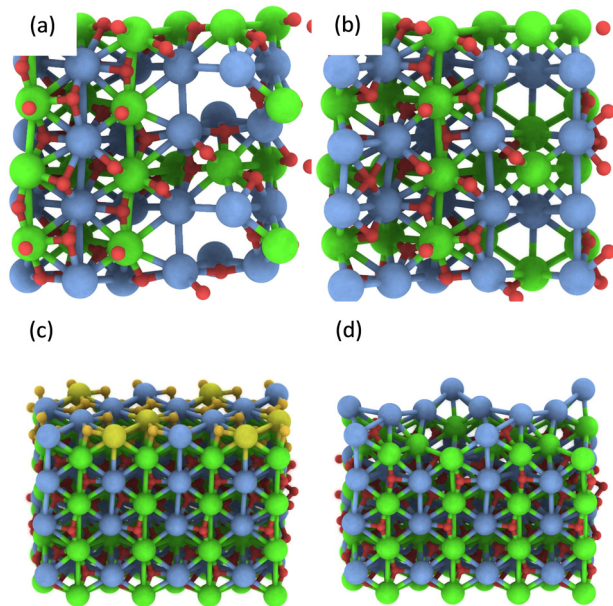


Fig. 6 The most energetically favourable structure of the CaZrO<sub>3</sub> bulk crystal from DFT calculations corresponding to the stoichiometry Ca<sub>12</sub>Zr<sub>10</sub>O<sub>28</sub> (a) and Ca<sub>11</sub>Zr<sub>12</sub>O<sub>26</sub> (CaZrO<sub>3</sub>-II) (b). (001) surface of CaZrO<sub>3</sub> corresponding to the stoichiometry Ca<sub>32</sub>Zr<sub>32</sub>O<sub>96</sub> (c). The yellow and orange spheres representing the Ca and O atoms were removed, creating a Ca<sub>29</sub>Zr<sub>32</sub>O<sub>69</sub> slab corresponding to the stoichiometry of the CaZrO<sub>3</sub>-II sample (d). See Fig. 2 for the colour code.

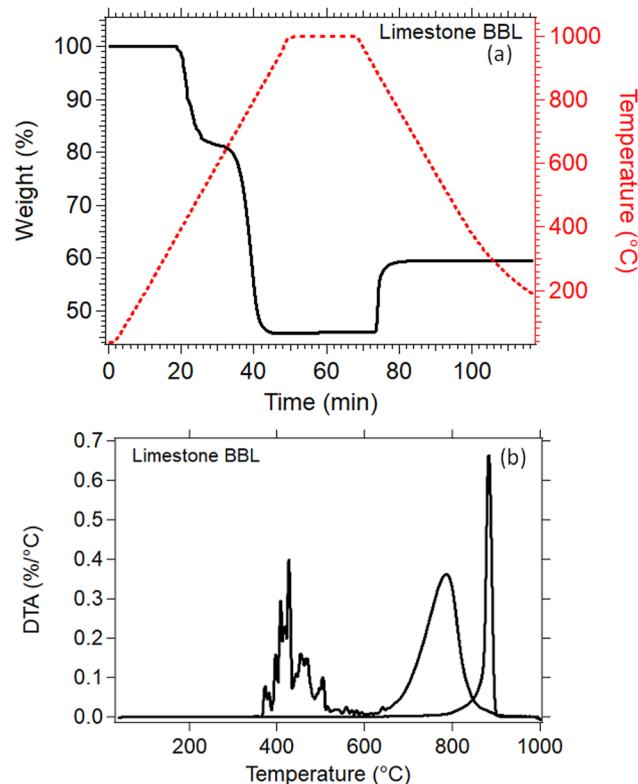


Fig. 7 (a) TGA of Lim BBL in N<sub>2</sub> environment up to 1000 °C (b) DTA of Lim BBL in N<sub>2</sub> environment up to 1000 °C.

20 minutes, and then cooled down to room temperature. No weight gain was observed during the isothermal period, indicating that the temperature was too high for the carbonation reaction to take place. While cooling under a 90% CO<sub>2</sub> atmosphere, a weight gain from 45% to 60% was observed due the absorption of CO<sub>2</sub> into CaO to form CaCO<sub>3</sub> (Fig. 7(a)). This reaction is also known as carbonation reaction, with an observed on-set temperature at 810 °C, a peak maximum at 884 °C and a completion at 900 °C (Fig. 7(b)). The weight gain for this reaction was only equal to 15 wt%, indicating that the carbonation reaction is incomplete (Fig. 7(a)).

### Thermochemical (calcination/carbonation) cycling and heat storage performance for all samples

For the thermochemical cycling, a constant temperature was chosen at 884 °C corresponding to the peak temperature of the carbonation reaction (Fig. 7(b)). The reason for not choosing two different temperatures for the calcination and carbonation step for the cycling experiment, was mainly to simplify the system. It is well known in the literature that the calcination reaction is faster in comparison to the carbonation reaction.<sup>29,65–67</sup> For this

reason, 10 minutes were chosen for the calcination step and 20 minutes for the carbonation step during cycling. In total, 40 cycles were applied on all samples. Their effective conversion and heat storage densities were calculated and presented in Fig. 8 and Table 5. During the first ten cycles, the effective conversions dropped for all seven samples, indicating that the carbonation reaction is incomplete at the end of each cycle. This can easily be observed in Fig. S1 (ESI<sup>†</sup>) where the comparison of the reaction kinetics for all seven samples is plotted, showing a complete reaction for the calcination reaction and an incomplete carbonation reaction. It is reported in the literature that the carbonation process takes place in two stages.<sup>63</sup> In the first stage, CO<sub>2</sub> diffuses at a high rate into the first layers of the CaO grains, and forms a CaCO<sub>3</sub> layer. This first stage is completed as soon as this CaCO<sub>3</sub> layer is formed around the CaO grains. In the second stage, the carbonation reaction is restricted by a solid-state diffusion of Ca<sup>2+</sup>, O<sup>2-</sup> and CO<sub>3</sub><sup>2-</sup> ions across the formed CaCO<sub>3</sub> layer, which significantly reduces the rate of the reaction. The purpose of using nanoadditives with high ionic conductivity like



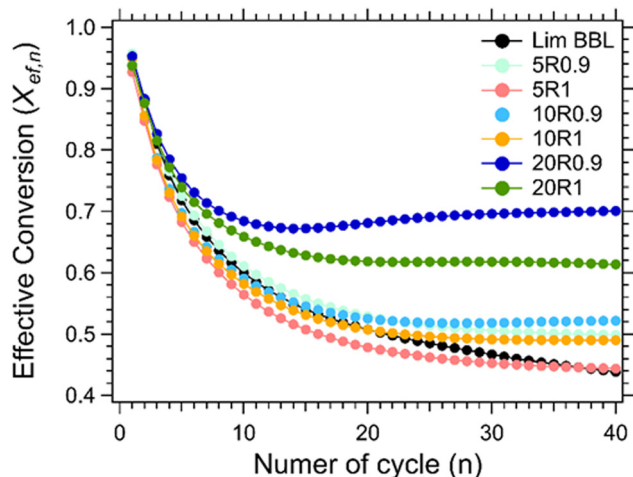


Fig. 8 Effective conversion vs number of cycle for Lim BBL with different percentages of  $\text{CaZrO}_3$ -I and  $\text{CaZrO}_3$ -II.

Table 5 Energy density ( $\text{kJ kg}^{-1}$ ) values of all samples after 10,20,30,40 cycles

# of cycles	Lim BBL	5R1	5R0.9	10R1	10R0.9	20R1	20R0.9
10	2257.9	2124.5	2300.2	2190.1	2223.7	2481.2	2577.7
20	1912.2	1802.2	1992.6	1910.8	1978.6	2328.7	2565.8
30	1758.9	1705.0	1905.6	1851.2	1952.1	2327.0	2622.0
40	1651.4	1671.1	1878.8	1845.4	1966.0	2311.2	2640.3

$\text{CaZrO}_3$  is to reduce these kinetic barriers by facilitating the ionic mobility necessary for the carbonation reaction to complete. After the first ten cycles, a relatively stable cyclic performance was observed for all samples. Samples Lim BBL and 5R1 had the lowest effective conversion value of  $\sim 0.44$  and a heat storage density of  $1651.4 \text{ kJ kg}^{-1}$  and  $1671.1 \text{ kJ kg}^{-1}$ . It is worth noticing that even though the same amount of nanoadditives (5 wt%  $\text{CaZrO}_3$ ) was used in sample 5R0.9, their effective conversion and heat storage density at the end of the 40th cycle was 0.50 and  $1878.8 \text{ kJ kg}^{-1}$ , indicating that the difference of ionic conductivity within the samples plays a significant role in the cycling performance. The same can be observed for the best performing samples, 20R1 and 20R0.9, where the amount of nanoadditives used is exactly the same (20 wt%) but their performance is significantly different. In detail, after 40 cycles sample 20R1 has effective conversion value equal to 0.61 and a heat storage density of  $2311.2 \text{ kJ kg}^{-1}$ . Whereas sample 20R0.9 has an effective conversion value equal to 0.70 and a heat storage density of  $2640.3 \text{ kJ kg}^{-1}$ .

### Ionic conductivity from a DFT perspective

Theoretical DFT calculations were carried out for a better understanding of the ionic conductivity mechanism in  $\text{CaZrO}_3$ . A series of static total energy calculations for a defective  $\text{CaZrO}_3$  with two a single missing O or Ca atoms, sampling migration paths for a single O or Ca between the two vacancies (Section S4, ESI<sup>†</sup>), revealed high migration barriers for both O (lowest barrier was 5.5 eV) and Ca (barrier at least 9.7 eV), Fig. 9.

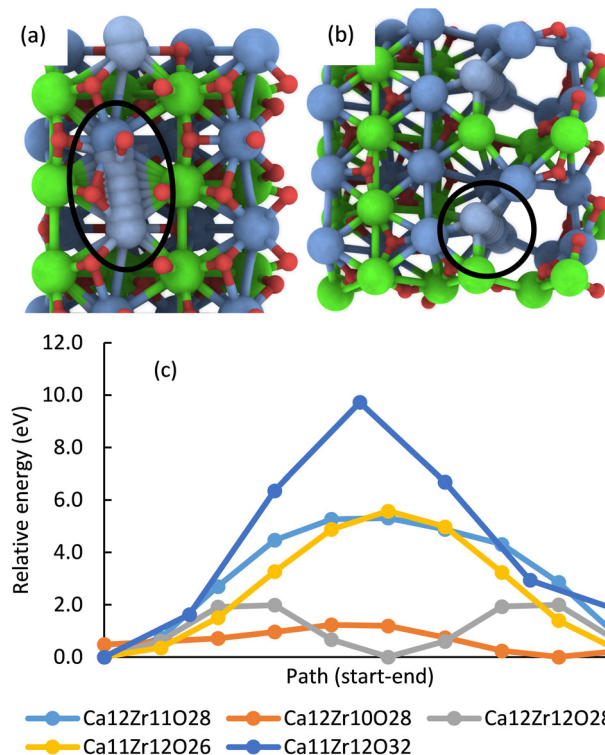


Fig. 9 The most energetically favourable migration path enclosed by the black line for a single Ca through a defective  $\text{CaZrO}_3$  crystal with the stoichiometry  $\text{Ca}_{11}\text{Zr}_{12}\text{O}_{32}$  (dark blue line in (c)) (a) and  $\text{Ca}_{12}\text{Zr}_{10}\text{O}_{28}$  (orange line in (c)) (b). Energy profile of migration paths of a single Ca in systems with a given element composition (c). The energy is relative to the lowest point on the system's profile. Migration is easier with increasing channel width (*cf.* the text) and even a very narrow channel reduces the barrier by almost half ( $\text{Ca}_{12}\text{Zr}_{10}\text{O}_{28}$ ,  $\text{Ca}_{11}\text{Zr}_{12}\text{O}_{26}$ , *cf.* Fig. S8–S11 in the ESI<sup>†</sup>).

In multi-defect systems that correspond to the experimental stoichiometry, the migration of atoms for the GS geometry through the entire supercell (from one boundary to the opposite), *i.e.*, through an endless channel (Section S5, ESI<sup>†</sup>) was investigated. In most of the studied systems, the lowest O migration barrier was reduced to 1.1–1.9 eV, for Ca it was in the range 1.2–5.6 eV (Fig. 9), and for Zr the barriers for the two considered paths were 3.5 eV and 5.4 eV.

It should be noted that the above calculations did not consider possible structural changes related to ion transport. However, it still gives us a picture of the potential acting on the fast-moving ion in the  $\text{CaZrO}_3$  system.

The reliability of this approach was examined against a commonly used technique for finding reaction paths, *i.e.*, the nudged elastic band (NEB) method.<sup>68,69</sup> As the input path for the NEB calculations of Ca migration, a significantly energetically unfavourable path used for the static calculations was chosen. During the NEB calculations, this path was corrected to the more energetically favourable Ca migration path, which was also found earlier by static calculations. Thus, it can be expected that even in static calculations, energy-favourable paths are described quite precisely, while paths with high energy barriers will be corrected in the NEB method.



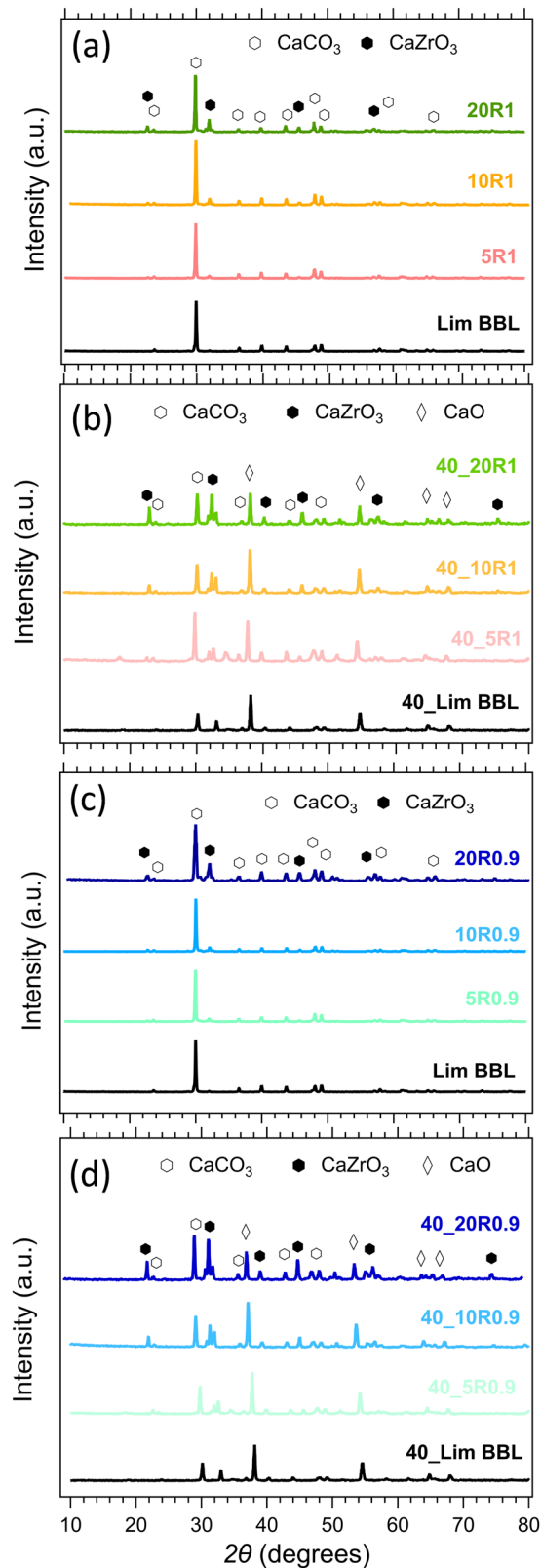


Fig. 10 Powder X-ray diffraction patterns of the LimBBL (Limestone waste) sample and  $\text{CaZrO}_3/\text{CaCO}_3$  mixture samples (a), (c) before and (b), (d) after 40 consecutive cycles.

Note also that the paths associated with low diffusion barriers are those farther from the wall of the migration channel, because the elemental composition of the wall determines the potential acting on the migrating atom.

Finally, the desorption of O into the vacuum requires significant energy, at least 6.7 eV, which is comparable to the defect formation energy of a single O vacancy, *i.e.*, 6.8 eV. Interestingly, in the presence of uncoordinated Ca atoms on the  $\text{CaZrO}_3$  surface, the first local maximum associated with O desorption is only 1.0 eV (Fig. S12, ESI<sup>†</sup>).

The desorption of the Ca atom from the surface was also investigated (Fig. S12, ESI<sup>†</sup>), and the energy required for this process (2.2–2.8 eV) is less than the defect formation energy of a single Ca vacancy (3.4 eV).

### Composition of Limestone waste and $\text{CaZrO}_3$ /Limestone mixture samples

The composition of all samples before and after cycling is presented in Fig. 10. It is noticeable that the dominant crystal phase in all as-prepared samples (Fig. 10(a) and (c)) is  $\text{CaCO}_3$ , including the Limestone waste, indicating that any impurities

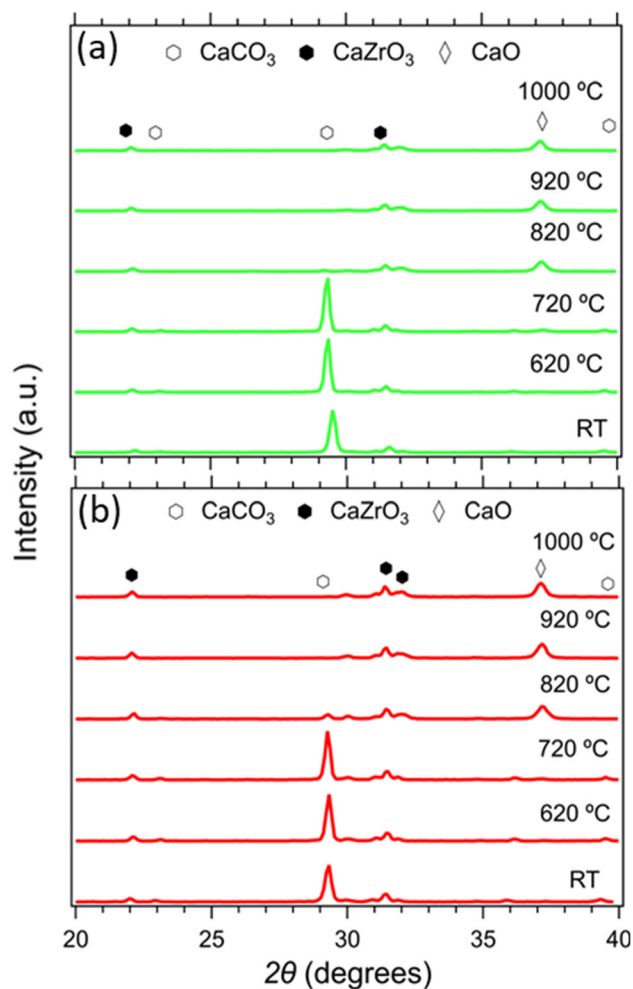


Fig. 11 *In situ* X-ray diffraction data of the 20R1 and 20R0.9 samples from room temperature to 1000 °C.



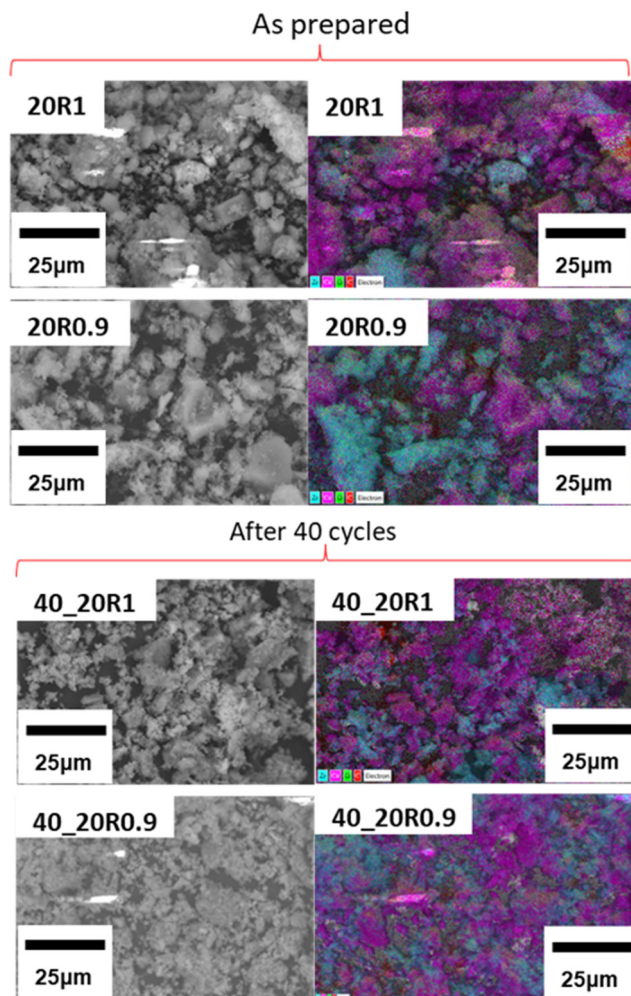


Fig. 12 EDS mapping of 20%  $\text{CaZrO}_3$  samples, before and after 40 cycles. Blue is for Zr, purple is for Ca, green is for O and red is for C.

present are in very low concentration and not detectable by X-ray diffraction. The diffraction peaks assigned to the secondary  $\text{CaZrO}_3$  phase for the mixture samples become more obvious as the  $\text{CaZrO}_3$  content increases, as expected. After 40 cycles (Fig. 10(b) and (d)) the dominant phase in all samples is CaO along with  $\text{CaCO}_3$  and  $\text{CaZrO}_3$ . No reaction products between  $\text{CaCO}_3$  and  $\text{CaZrO}_3$  upon cycling were observed, also confirmed by the *in situ* X-ray diffraction data presented in Fig. 11. Indicating, that  $\text{CaZrO}_3$  is chemically stable upon cycling.

Table 6 BET surface area of samples in  $\text{m}^2 \text{g}^{-1}$  before and after cycling

Sample ID	Before cycling	After cycling
Lim BBL	$1.03 \pm 0.1$	$4.53 \pm 0.5$
5R1	$1.15 \pm 0.1$	$3.77 \pm 0.4$
10R1	$2.20 \pm 0.2$	$4.81 \pm 0.5$
20R1	$2.70 \pm 0.3$	$3.29 \pm 0.3$
5R0.9	$2.09 \pm 0.2$	$1.56 \pm 0.2$
10R0.9	$1.91 \pm 0.2$	$5.10 \pm 0.5$
20R0.9	$2.10 \pm 0.2$	$3.89 \pm 0.4$

## Morphology and physisorption analysis of Limestone waste and $\text{CaZrO}_3/\text{CaCO}_3$ mixture samples

EDS mapping and BET specific surface area analysis were carried out on all samples both before and after cycling to evaluate the morphological changes that take place upon cycling (Fig. 12, Fig. S2, S3, ESI† and Table 6). In Fig. 12 the SEM micrographs of the Lim BBL, 20R1 and 20R0.9 samples are presented, both before and after their 40 calcination/carbonation cycles. It can be observed that all three samples after cycling exhibit particles smaller in size in comparison to the ones before cycling, as reflected also in their calculated BET surface areas (Table 6), with the 40\_10R1 and 40\_10R0.9 samples having the highest BET surface areas. This may be due to some physical redistribution of the Limestone grains and the  $\text{CaZrO}_3$  nanoadditives upon cycling; as noticed in Fig. 12 (after 40 cycles) where the  $\text{CaZrO}_3$  nanoparticles seem to be better distributed throughout the sample after cycling. These observations are also reflected for the other mixture samples as seen in Fig. S2 and S3 (ESI†). The very low specific surface area of all as-prepared samples (Table 6) is due to the fact that these samples were not ball milled and were used as-supplied. The average particle size of the Limestone waste was  $2.28 \mu\text{m}$  as calculated from its associated SEM image (Fig. S4, ESI†).

## Conclusions

The cycling performance of Limestone was improved by designing  $\text{CaZrO}_3$  nanoadditive.  $\text{CaZrO}_3$  samples with two different Ca:Zr ratio was successfully synthesized by wet precipitation method. XRD analysis confirm the synthesis of  $\text{CaZrO}_3$ .  $\text{CaZrO}_3$  nanoparticles were observed in SEM and TEM images. XPS analysis revealed that, the percentage of  $\text{O}_{\text{vac}}$  of the  $\text{CaZrO}_3$ -I and  $\text{CaZrO}_3$ -II samples were 23.43% and 28.58% respectively. Structures corresponding to the experimental stoichiometry were investigated by DFT calculations. They revealed that multiple defects are formed in  $\text{CaZrO}_3$ , and their presence improves the ionic conductivity of this material. Out of all mixture samples the one with 20%  $\text{CaZrO}_3$ -II exhibited the best performance with an effective conversion of 0.7 and energy density of  $2640 \text{ kJ kg}^{-1}$ . The second best performing mixture sample was the one with 20%  $\text{CaZrO}_3$ -I; exhibiting an effective conversion of 0.61 and energy density of  $2311 \text{ kJ kg}^{-1}$ . The XRD analysis of all samples after cycling confirmed that  $\text{CaZrO}_3$  did not react with Limestone. The SEM/EDS analysis of the samples after cycling showed a better distribution of Limestone and  $\text{CaZrO}_3$  particles; which can be responsible for stable cycling performance.

## Conflicts of interest

There are no conflicts to declare.

## Acknowledgements

MVS acknowledges the financial support from the UCD Ad Astra Fellowship Programme and the Technology Transfer



Strengthening Initiative Programme from Enterprise Ireland (reference grant number 68001). RA acknowledges the financial support from the UCD Ad Astra Studentship Programme. All authors would like to thank Prof. James Sullivan and Kristy Stanley for providing access to the TA Q500 Thermogravimetric analyser located at the UCD School of Chemistry. The work in Olomouc was supported by the Operational Programme for Research, Development and Education of the European Regional Development Fund (Project no. CZ.02.1.01/0.0/0.0/16\_019/0000754 of the Ministry of Education, Youth and Sports of the Czech Republic). JN acknowledges support by Palacký University Olomouc (project IGA\_PrF\_2022\_019). The IT4Innovations National Supercomputing Center is gratefully acknowledged for providing generous computational resources supported by the Ministry of Education, Youth and Sports of the Czech Republic through the e-INFRA CZ (No. 90140). All authors would like to thank Bennettsbridge Limestone Quarries, Ireland for providing Limestone waste for this study.

## References

- I. Irena, *Report, International Renewable Energy Agency*, Abu Dhabi, 2018.
- Z. Yuan, L. Liang, Q. Dai, T. Li, Q. Song, H. Zhang, G. Hou and X. Li, *Joule*, 2022, **6**, 884–905.
- J. Haas, L. Prieto-Miranda, N. Ghorbani and C. Breyer, *Renewable Energy*, 2022, **181**, 182–193.
- Y. Yang, Y. Li, X. Yan, J. Zhao and C. Zhang, *Energies*, 2021, **14**, 6847.
- R. Paul, M. Wang and A. Roy, *ACS Appl. Nano Mater.*, 2020, **3**, 10418–10426.
- U. Pelay, L. Luo, Y. Fan, D. Stitou and M. Rood, *Renewable Sustainable Energy Rev.*, 2017, **79**, 82–100.
- J. Cot-Gores, A. Castell and L. F. Cabeza, *Renewable Sustainable Energy Rev.*, 2012, **16**, 5207–5224.
- A. I. Fernandez, M. Martínez, M. Segarra, I. Martorell and L. F. Cabeza, *Sol. Energy Mater. Sol. Cells*, 2010, **94**, 1723–1729.
- C. Wani and P. Kumar Loharkar, *Mater. Today: Proc.*, 2017, **4**, 10264–10267.
- A. Carro, R. Chacartegui, C. Ortiz and J. Becerra, *Energy*, 2022, 125064.
- P. Pardo, A. Deydier, Z. Anxionnaz-Minvielle, S. Rougé, M. Cabassud and P. Cognet, *Renewable Sustainable Energy Rev.*, 2014, **32**, 591–610.
- K. Wang, T. Yan, R. Li and W. Pan, *J. Energy Storage*, 2022, **50**, 104612.
- N. R. Rhodes, A. Barde, K. Randhir, L. Li, D. W. Hahn, R. Mei, J. F. Klausner and N. AuYeung, *ChemSusChem*, 2015, **8**, 3793–3798.
- Q. Zhao, J. Lin, H. Huang, Z. Xie and Y. Xiao, *J. Energy Storage*, 2022, **50**, 104259.
- R. Han, S. Xing, X. Wu, C. Pang, S. Lu, Y. Su, Q. Liu, C. Song and J. Gao, *Renewable Energy*, 2022, **181**, 267–277.
- N. Amghar, C. Ortiz, A. Perejón, J. M. Valverde, L. P. Maqueda and P. E. S. Jiménez, *Sol. Energy Mater. Sol. Cells*, 2022, **238**, 111632.
- X. Qu, Y. Li, P. Li, Q. Wan and F. Zhai, *Front. Mater. Sci.*, 2015, **9**, 317–331.
- M. Hirscher, V. A. Yartys, M. Baricco, J. Bellosta von Colbe, D. Blanchard, R. C. Bowman, D. P. Broom, C. E. Buckley, F. Chang, P. Chen, Y. W. Cho, J.-C. Crivello, F. Cuevas, W. I. F. David, P. E. de Jongh, R. V. Denys, M. Dornheim, M. Felderhoff, Y. Filinchuk, G. E. Froudakis, D. M. Grant, E. M. Gray, B. C. Hauback, T. He, T. D. Humphries, T. R. Jensen, S. Kim, Y. Kojima, M. Latroche, H.-W. Li, M. V. Lototsky, J. W. Makepeace, K. T. Møller, L. Naheed, P. Ngene, D. Noréus, M. M. Nygård, S.-I. Orimo, M. Paskevicius, L. Pasquini, D. B. Ravnsbæk, M. Veronica Sofianos, T. J. Udovic, T. Vegge, G. S. Walker, C. J. Webb, C. Weidenthaler and C. Zlotea, *J. Alloys Compd.*, 2020, **827**, 153548.
- P. Larpruenrudee, N. S. Bennett, Y. Gu, R. Fitch and M. S. Islam, *Sci. Rep.*, 2022, **12**, 1–16.
- C. Comanescu, *Int. J. Mol. Sci.*, 2022, **23**, 7111.
- M. Schmidt and M. Linder, *Appl. Energy*, 2017, **203**, 594–607.
- K. T. Møller, T. D. Humphries, A. Berger, M. Paskevicius and C. E. Buckley, *Chem. Eng. J. Adv.*, 2021, **8**, 100168.
- K. E. N'Tsoukpoe, H. Liu, N. Le Pierrès and L. Luo, *Renewable Sustainable Energy Rev.*, 2009, **13**, 2385–2396.
- A. Martínez, Y. Lara, P. Lisbona and L. M. Romeo, *Int. J. Greenhouse Gas Control*, 2012, **7**, 74–81.
- A. Bayon, R. Bader, M. Jafarian, L. Fedunik-Hofman, Y. Sun, J. Hinkley, S. Miller and W. Lipiński, *Energy*, 2018, **149**, 473–484.
- C. Prieto, P. Cooper, A. I. Fernández and L. F. Cabeza, *Renewable Sustainable Energy Rev.*, 2016, **60**, 909–929.
- K. T. Møller, A. Berger, M. Paskevicius and C. E. Buckley, *J. Alloys Compd.*, 2022, **891**, 161954.
- Y. Zhou, Z. Zhou, L. Liu, X. She, R. Xu, J. Sun and M. Xu, *Energy Fuels*, 2021, **35**, 18778–18788.
- K. T. Møller, A. Ibrahim, C. E. Buckley and M. Paskevicius, *J. Mater. Chem. A*, 2020, **8**, 9646–9653.
- Z. Sun, S. Luo, P. Qi and L.-S. Fan, *Chem. Eng. Sci.*, 2012, **81**, 164–168.
- C. Li, Y. Li, C. Zhang, Y. Dou, Z. He and J. Zhao, *Fuel Process. Technol.*, 2022, **237**, 107444.
- X. Tian, S. Lin, J. Yan and C. Zhao, *Chem. Eng. J.*, 2022, **428**, 131229.
- A. Mathew, N. Nadim, T. T. Chandratilleke, M. Paskevicius, T. D. Humphries and C. E. Buckley, *Sol. Energy*, 2022, **241**, 262–274.
- H. Sun, Y. Li, X. Yan, J. Zhao and Z. Wang, *Appl. Energy*, 2020, **263**, 114650.
- A. A. Khosa, T. Xu, B. Xia, J. Yan and C. Zhao, *Sol. Energy*, 2019, **193**, 618–636.
- T. Richardson, R. K. Vijayaraghavan, P. McNally and M. V. Sofianos, Available at SSRN 4156637.
- A. A. Khosa and C. Zhao, *Sol. Energy*, 2019, **188**, 619–630.
- X. Chen, X. Jin, Z. Liu, X. Ling and Y. Wang, *Energy*, 2018, **155**, 128–138.
- J. M. Valverde, M. Barea-López, A. Perejón, P. E. Sánchez-Jiménez and L. A. Pérez-Maqueda, *Energy Fuels*, 2017, **31**, 4226–4236.



- 40 B. Sarrión, A. Perejón, P. E. Sánchez-Jiménez, L. A. Pérez-Maqueda and J. M. Valverde, *J. CO2 Util.*, 2018, **28**, 374–384.
- 41 B. Sarrion, P. E. Sanchez-Jimenez, A. Perejon, L. A. Perez-Maqueda and J. M. Valverde, *ACS Sustainable Chem. Eng.*, 2018, **6**, 7849–7858.
- 42 S. M. Alay-e-Abbas, S. Nazir, S. Cottenier and A. Shaukat, *Sci. Rep.*, 2017, **7**, 8439.
- 43 P. Han, H. Lv, X. Li, S. Wang, Z. Wu, X. Li, Z. Mu, X. Li, C. Sun, H. Wei and L. Ma, *Catal. Sci. Technol.*, 2021, **11**, 3697–3705.
- 44 M. Zhao, M. Bilton, A. P. Brown, A. M. Cunliffe, E. Dvininov, V. Dupont, T. P. Comyn and S. J. Milne, *Energy Fuels*, 2014, **28**, 1275–1283.
- 45 M. Pollet, S. Marinel and G. Desgardin, *J. Eur. Ceram. Soc.*, 2004, **24**, 119–127.
- 46 C. S. Prasanth, H. Padma Kumar, R. Pazhani, S. Solomon and J. K. Thomas, *J. Alloys Compd.*, 2008, **464**, 306–309.
- 47 G. Kresse and J. Furthmüller, *Comput. Mater. Sci.*, 1996, **6**, 15–50.
- 48 G. Kresse and J. Hafner, *Phys. Rev. B: Condens. Matter Mater. Phys.*, 1993, **47**, 558–561.
- 49 G. Kresse and J. Furthmüller, *Phys. Rev. B: Condens. Matter Mater. Phys.*, 1996, **54**, 11169–11186.
- 50 G. Kresse and J. Hafner, *Phys. Rev. B: Condens. Matter Mater. Phys.*, 1994, **49**, 14251–14269.
- 51 G. Kresse and D. Joubert, *Phys. Rev. B: Condens. Matter Mater. Phys.*, 1999, **59**, 1758–1775.
- 52 P. E. Blöchl, *Phys. Rev. B: Condens. Matter Mater. Phys.*, 1994, **50**, 17953–17979.
- 53 J. P. Perdew, K. Burke and M. Ernzerhof, *Phys. Rev. Lett.*, 1996, **77**, 3865–3868.
- 54 J. P. Perdew, K. Burke and M. Ernzerhof, *Phys. Rev. Lett.*, 1997, **78**, 1396.
- 55 S. Grimme, J. Antony, S. Ehrlich and H. Krieg, *J. Chem. Phys.*, 2010, **132**, 154104.
- 56 K. Momma and F. Izumi, *J. Appl. Crystallogr.*, 2011, **44**, 1272–1276.
- 57 <https://github.com/wwwtyro/speck> (accessed 14/02/2022).
- 58 P. Han, X. Li, C. Jin, X. Tan, W. Sun, S. Wang, F. Ding, X. Li, H. Jin and C. Sun, *Chem. Eng. J.*, 2022, **429**, 132218.
- 59 R. S. André, S. M. Zanetti, J. A. Varela and E. Longo, *Ceram. Int.*, 2014, **40**, 16627–16634.
- 60 R. Koirala, K. R. Gunugunuri, S. E. Pratsinis and P. G. Smirniotis, *J. Phys. Chem. C*, 2011, **115**, 24804–24812.
- 61 M. López Granados, A. Gurbani, R. Mariscal and J. L. G. Fierro, *J. Catal.*, 2008, **256**, 172–182.
- 62 B. Luo, H. Dong, D. Wang and K. Jin, *J. Am. Ceram. Soc.*, 2018, **101**, 3460–3467.
- 63 B. Luo, *J. Appl. Phys.*, 2017, **122**, 195104.
- 64 G. Cabello, L. Lillo, C. Caro, G. E. Bueno-Core, B. Chornik, M. Flores, C. Carrasco and C. A. Rodriguez, *Ceram. Int.*, 2014, **40**, 7761–7768.
- 65 A. M. López-Periago, J. Fraile, P. López-Aranguren, L. F. Vega and C. Domingo, *Chem. Eng. J.*, 2013, **226**, 357–366.
- 66 Y. A. Criado, B. Arias and J. C. Abanades, *Ind. Eng. Chem. Res.*, 2018, **57**, 12595–12599.
- 67 B. R. Stanmore and P. Gilot, *Fuel Process. Technol.*, 2005, **86**, 1707–1743.
- 68 G. Mills and H. Jónsson, *Phys. Rev. Lett.*, 1994, **72**, 1124–1127.
- 69 G. Mills, H. Jónsson and G. K. Schenter, *Surf. Sci.*, 1995, **324**, 305–337.

